Coupling ideality of free electrons with photonic integrated waveguides

Guanhao Huang,[1,2,*] Nils J. Engelsen,[1,2] Ofer Kfir,[3] Claus Ropers,[4,5] and Tobias J. Kippenberg[1,2]

[1] *Swiss Federal Institute of Technology Lausanne (EPFL), CH-1015 Lausanne, Switzerland*
[2] *Center for Quantum Science and Engineering, EPFL, CH-1015 Lausanne, Switzerland*
[3] *School of Electrical Engineering, Tel Aviv University, 69978, Tel Aviv, Israel*
[4] *Max Planck Institute of Multidisciplinary Sciences, D-37077 Göttingen, Germany*
[5] *Georg-August-Universität Göttingen, D-37077 Göttingen, Germany*

Recently, integrated photonics has brought new capabilities to electron microscopy and been used to demonstrate efficient electron phase modulation and electron-photon correlations. Here, we quantitatively analyze the interaction strength between a free electron and a photonic integrated circuit with a heterogeneous structure. We adopt a dissipative QED treatment and show that with proper electron beam positioning and waveguide geometry, one can achieve near-unity coupling ideality to a well-defined spatial-temporal waveguide mode. Furthermore, we show that the frequency and waveform of the coupled mode can be tailored to the application. These features show that photonic integrated waveguides are a promising platform for free-electron quantum optics with applications like high-fidelity electron-photon entanglement, heralded single-electron and photon state synthesis.

Quantum coherent coupling between disparate physical systems is required for a future quantum network [1]. Proposed architectures generally use photonic links [2] to connect different systems due to the potential for long-range transmission through optical fibers and robustness to decoherence from thermal environments. Photonic links have been realized in systems ranging from superconducting qubits [3, 4], solid state spins [5, 6], ultra coherent mechanics [7, 8], and atomic systems [9–13], where each offers unique features and advantages to be utilized in quantum networks. One key aspect of all these systems is the ability to enact high-fidelity quantum control of the interaction with well-defined optical modes.

In the field of electron microscopy, interactions between free electrons and photons have been widely explored in both stimulated [14–21] and spontaneous processes [15, 22–24] enhanced by phase-matched interaction and optical resonance [25–29]. There have also been many proposals [30–34] exploring the unique quantum properties of electron-photon states. However, it is still an open question whether high-fidelity quantum control of this hybrid quantum system can be realized.

High-fidelity quantum control requires high coupling strength between free electrons and optical vacuum fields, and low dissipation to keep decoherence at a minimum. The interaction mechanisms and their coupling strengths differ substantially between different physical platforms, which can be categorized into metallic [17] and dielectric structures [19, 25, 29, 35, 36]. For nanophotonic particles, the short attosecond-long interaction time promotes the use of absorbing materials, such as plasmonic structures [37]. The collective electronic response amplifies the interaction, while at the same time bringing retardation and dissipation, which is not ideal for quantum-coherent manipulation of electrons with optical states. On the other hand, transparent dielectrics, for which the coupling is enhanced by an extended interaction length, offer a paradigm shift in free-electron quantum optics due to their low optical dissipation and instant electronic response. Instead of enhancing the interaction by lossy media, optical modes supported by the dielectric structures interact with the free electron by the relativistic field retardation effect [38], which results in a purely parametric interaction ideally suited for high-fidelity quantum control.

Photonic integrated circuits have only entered the picture very recently [29, 39], and have several advantages for free-electron quantum optical experiments. Firstly, integrated photonics enables exquisite control of the optical properties of waveguides [40]. The nearly lossless guided modes [41] and high-fidelity output fiber coupling [42] facilitate coupling to both on-chip [5–8] and fiber-coupled quantum systems [3, 10–13]. Additional capabilities are provided by well-established on-chip optical elements such as tunable beam splitters and phase shifters [43], which offer high-fidelity optical state manipulation and characterization [44].

High-fidelity interaction between quantum systems mediated by the electron-photon interaction requires high-ideality coupling to a well-defined single optical mode [45]. However, due to the presence of waveguide substrates, contributions from parasitic coupling to auxiliary spatial modes limit the fidelity of the interaction. To quantify the infidelity caused by this parasitic coupling, the conventional quantum optical modal decomposition method commonly used in previous works [17, 29, 31, 32] is practically inconvenient to use since there is an infinite number of optical modes supported by the dielectric structures that the electrons can interact with.

Here, we adopt a dissipative QED treatment [46] in the lossless limit to circumvent the need to address all the modes individually, which allows quantitative analysis of the parasitic coupling contributions and the coupling ideality to the target mode. From the analysis, we find that with appropriate waveguide structure design and electron beam positioning, we can achieve optical

* guanhao.huang@epfl.ch

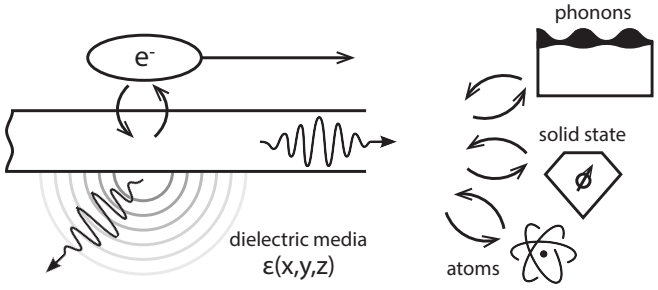

FIG. 1. Illustration of the electron-photon inelastic scattering process mediated by a dielectric waveguide. When the electron passes by a dielectric waveguide structure with a given dielectric permittivity distribution $\epsilon(x, y, z)$, the material dielectric dipoles exert a backaction field (force) on the electron, resulting in correlated electron energy loss and optical field emission in both the guided waveguide modes and non-guided bulk modes. High-ideality coupling to a low-loss waveguide mode is required for interaction with other quantum systems through optical links.

frequency tuning and waveform shaping of the output optical state, and most importantly, near-unity, single-mode coupling ideality, enabling high-fidelity quantum control of electron-photon interactions.

I. THEORY BASICS

The interaction between free electrons and optical modes at a dielectric surface can be understood in a microscopic picture, see Fig.1. When an electron passes near the surface of a dielectric structure, the electric field of the flying electron polarizes the dipoles in the structure. As a result, these dipoles generate oscillating electromagnetic fields that cause backaction Coulomb forces on the electron which change the electron energy. In the conventional quantum optical modal decomposition picture commonly used in the cavity QED community, this can be interpreted as the interaction between the free electrons and the optical vacuum fields of the modes supported by the dielectric structure [47].

In the case of photonic integrated circuits, the complex dielectric environment can degrade the fidelity of the electron-photon interaction with the target waveguide mode, e.g., through parasitic coupling to other optical mode families and other non-guided spatial modes supported by the generally open-ended dielectric substrates. It is impractical to use the conventional modal decomposition method [17] to account for the infinite number of interacting spatial optical modes. Instead, we use a three-dimensional QED treatment [46] (see Appendix B for QED details, and Appendix D for its correspondence to the modal decomposition), which takes into account all the possible coupling contributions from different modes. This formalism, derived using the fluctuation-dissipation theorem, was previously used when analyzing electron energy loss probabilities with dissipative materials [15]. Here, we use it for dispersive dielectric materials, i.e. the studied wavelength range is far from material absorption bands, which simplifies the simulation by not requiring knowledge of the imaginary part of the dielectric permittivity.

The problem can be formulated as the interaction between propagating free electrons and optical fields $\hat{\mathbf{A}}(\mathbf{r}, \omega)$ (instead of the specified optical modes) at frequencies ω, with the scattering matrix [31, 45]

$$\hat{S} = e^{i\hat{\chi}} \exp\left[\int d\omega g_\omega \hat{b}_\omega^\dagger \hat{a}_\omega - h.c.\right], \tag{1}$$

where the phase operator $\hat{\chi}$ acts only on the electron degrees of freedom, and is associated with the Aharonov–Bohm effect of the vector potential [48]. Traveling photon ladder operators $\hat{a}_\omega$ and electron operators $\hat{b}_\omega$ characterize the energy exchanges between the electron and the optical field at a given optical frequency ω in an energy-conserved manner. The interaction with the vacuum optical fields results in transitions into lower electron energy states with energy differences of $\hbar\omega$. We define the electron-photon coupling strength at a given photon energy $\hbar\omega$ in terms of the vacuum coupling strength g_ω as $\Gamma(\omega) = |g_\omega|^2$. In the limit where $\Gamma(\omega) \ll 1$, the $\Gamma(\omega)$ is also equivalent to the electron energy loss probability per unit optical frequency of the dielectric media measured in electron energy loss spectroscopy (EELS). Assuming the electron beam is oriented in direction $\hat{\mathbf{z}}$ at transverse coordinate $\mathbf{R}_0$, the coupling strength is [15]

$$\Gamma(\mathbf{R}_0, \omega) = \frac{4e^2}{\hbar} \iint dz dz' \\ \mathrm{Re}[ie^{i\frac{\omega(z-z')}{v_e}} G_{zz}(\mathbf{R}_0, z; \mathbf{R}_0, z'; \omega)], \tag{2}$$

where $G(\mathbf{r}, \mathbf{r}', \omega)$ is the dyadic Green function (Green tensor) of the classical Maxwell equation

$$\nabla \times \nabla \times G(\mathbf{r}, \mathbf{r}', \omega) - \frac{\omega^2}{c^2}\epsilon(\mathbf{r}, \omega) G(\mathbf{r}, \mathbf{r}', \omega) = -\mu_0 \delta(\mathbf{r} - \mathbf{r}')$$

which describes the field response at $\mathbf{r}$ to a point current excitation at $\mathbf{r}'$. The integral kernel $e^{i(z-z')\omega/v_e}$ enforces the phase-matching condition at electron velocity v_e, which is especially important to consider for prolonged interaction with dielectric waveguide structures. At this point, the problem of retrieving the coupling to an infinite number of spatial optical modes reduces to solving the Green tensor $G(\mathbf{r}, \mathbf{r}', \omega)$ of the dielectric environment $\epsilon(\mathbf{r}, \omega)$ of interest. In most previous works on EELS of nanostructures [15], the materials (e.g. metals) exhibit delayed material response, resulting in material absorption, which is the dominant contribution to the main electron energy loss channels. The dielectric materials we study here are transparent in the optical frequency bands of interest. In this sense, we can safely set $\mathrm{Im}\{\epsilon(\mathbf{r}, \omega)\} \to 0$, which corresponds to instantaneous dielectric dipole response. For materials with sufficiently

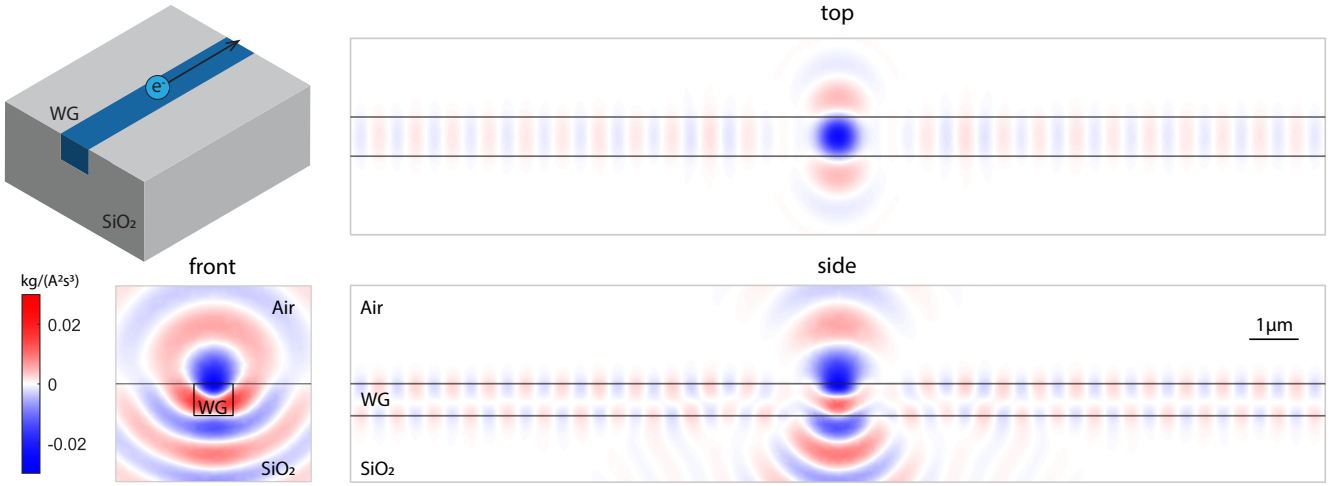

FIG. 2. Spatial pattern of $\mathrm{Im}[G_{zz}(\mathbf{r}, \mathbf{r}_0, \omega)]$ for the case of a Si_3N_4waveguide embedded in a silica substrate. In addition to emission into the substrate and free space, some guided modes in the waveguide are also excited by the oscillating electric current dipole, and forms a beating spatial pattern amongst guided modes along the waveguide direction.

low absorption, which are used for integrated waveguides designed to guide optical fields, the interaction is purely contributed from the relativistic field retardation effect [38] and prohibits energy and momentum transfer to the material, avoiding loss of coherence. It is in this sense that the whole process of electron interacting with dielectric waveguide is *parametric* in nature.

II. QUANTITATIVE ANALYSIS OF ELECTRON-PHOTON INTERACTION

As an example, here we quantitatively investigate the electron-photon coupling mediated by an integrated Si_3N_4waveguide embedded in a silica substrate without top cladding (the bottom silicon substrate not considered). This type of structure has been used in recent investigations of both stimulated phase-matched interactions [29] and spontaneous inelastic scattering [39] between free electrons and the evanescent field of a photonic-chip-based optical microresonator.

Since all the physical quantities we are interested in can be related to the Green tensor of the classical Maxwell equation given the dielectric structure of interest, we numerically solved the relevant Green tensor component $G_{zz}(\mathbf{r}, \mathbf{r}', \omega)$ of an infinitely long optical waveguide with FEM (see Appendix E for details on the simulation method). The spatial map of the Green function is illustrated in Fig. 2. The Green function can be understood intuitively as the Fourier component of the optical field at frequency ω that is excited at position $\mathbf{r}$ by the propagating electron at position $\mathbf{r}'$, whereas the phase matching condition determines whether this field constructively or destructively builds up at a given electron velocity. Given the expression of coupling strength from Eq. (2), it can be understood that with the optimal phase-matching condition, the coupling strength at a given optical frequency scales quadratically with the interaction length, a unique feature of guided modes co-propagating with the flying electron. For the spatial modes in the substrate bulk, the excited field is localized around the electron position. Without the benefit of constructive interference from co-propagation with the flying electron, their intensity only scales linearly with respect to interaction length.

From Eq. (2), we calculate and show the electron-photon vacuum coupling strength in Fig. 3 as a function of electron velocity for optical wavelengths ranging from 780 nm to 2.5 μm (the frequency bands where all relevant material properties are well known), which covers most of the frequency bands that are of general interest.

The coupling to waveguide modes scales quadratically with respect to interaction length under the optimal phase matching condition, which would cause broadband emission into the guided modes of a dispersion-free waveguide. In reality, waveguide modal dispersion implies phase-mismatched interaction at most optical frequencies, and results in finite coupling bandwidths that scale inversely proportional to the interaction length for different optical mode families as shown in Fig.3. It is difficult to design waveguides made of dispersive materials to have zero modal dispersion, which limits the total interaction strength of a given mode family,

$$|g_m|^2 \approx \int_{\Delta\omega_m} d\omega |g_\omega|^2, \tag{3}$$

in the mode's frequency window $\Delta\omega_m$ to scale linearly with interaction length and inversely with modal dispersion. Their peak coupling strengths, however, still maintain the quadratic scaling as the phase-matching condition is optimal.

Since the coupling to each mode family has a finite bandwidth, we define discrete spatial-temporal optical

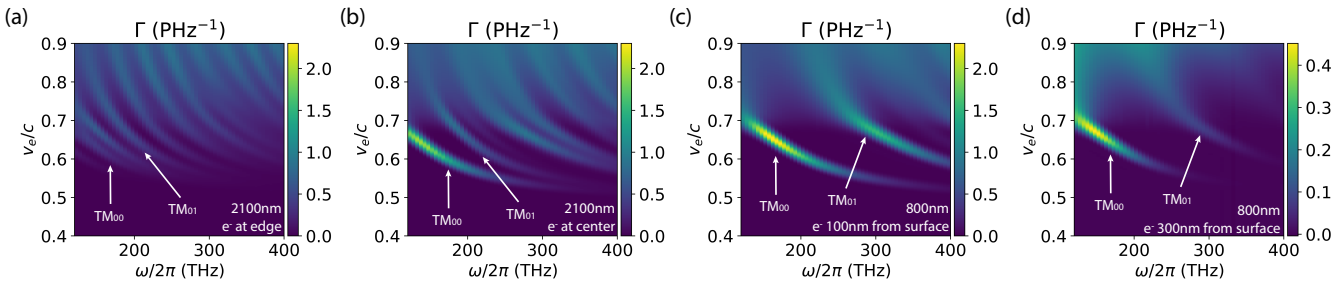

FIG. 3. Electron-photon coupling spectrum with 50 μm interaction length for different waveguide geometries and electron positioning. The coupling spectrum is plotted as a function of both electron velocity v_e and optical frequency ω. The waveguides have a thickness of 650 nm, and widths of **(a-b)** 2.1 μm and **(c-d)** 800 nm, and are embedded in a silica substrate. Coupling to different waveguide mode families appears as multiple coupling bands. Coupling ideality to the target TM_{00} mode is improved by changing the electron beam transverse position from waveguide edge (100 nm from surface) **(a)** to waveguide center **(b)**, from multimode waveguide **(b)** to single mode waveguide **(c)**, and moving further away (300 nm from surface) **(d)** from the waveguide surface. The waveguide widths and the relative positions of the electron beam are also labeled at the lower right corner of the panels.

modes $\hat{a}_m$ associated with different waveguide mode families from the waveguide continuum based on the coupling strengths $g_{m,\omega}$ of the interaction (details see Appendix D). Then, from the results shown in Fig.3, we can quantitatively evaluate the total coupling strengths $|g_m|^2$ to different mode family modes $\hat{a}_m$. As an example, for the quasi-TM_{00} mode of the 800 nm wide waveguide shown in Fig.3(c), for an electron trajectory 100 nm above the waveguide surface, a near unity coupling strength of $|g_{TM_{00}}|^2 \sim 1$ can be achieved with just 100 μm of interaction length at a electron velocity of $v_e/c = 0.65$ (a kinetic energy of 160 keV). The 100 nm gap distance and 100 μm e-beam propagation length are experimentally feasible and demonstrated in [39].

III. COUPLING IDEALITY

For free-electron quantum optics experiments, it is beneficial to have high-fidelity coupling to a single optical mode. It is therefore important to quantitatively understand the influence of competing waveguide modes on the interaction fidelity for a given waveguide configuration, and how one can approach unity coupling ideality by a proper choice of waveguide geometry and material, and electron beam positioning and velocity. Since the lowest order TM_{00} mode is generally the most strongly coupled and and is the most spectrally isolated mode, we target unity coupling ideality, defined by the coupling fraction

$$I \equiv |g_{TM_{00}}|^2 / \int d\omega |g_\omega|^2, \tag{4}$$

to the TM_{00} mode.

With a multimode waveguide, shown in Fig. 3(a-b), the effective mode index difference between the fundamental mode and higher order modes is relatively weak at the same optical frequency, which leads to multimode electron-photon interaction within a given frequency band. When the waveguide cross-section is reduced (referred to as *single mode* waveguide), shown in Fig.3(c), one can enhance the mode index contrast. As a result, the mode frequency spacing is increased, such that the coupled fundamental modes are better isolated. Since most transmission electron microscopes (TEMs) have an energy resolution around 0.5 eV (120 THz in optical frequency), it is important to create a large frequency spacing between the phase-matched optical modes so that the interaction with individual modes can be energy resolved.

The evanescent field of the coupled higher order modes decay faster than that of the coupled fundamental mode, as a result of the higher optical frequency. In Fig. 3(d), we show that one can further enhance the coupling contrast between fundamental mode and higher order modes by placing the electron beam further away (200 nm) from the waveguide surface. In this way, the interaction exponentially favors the fundamental mode, at the expense of weaker interaction strength $|g_{TM_{00}}|^2$ which can be compensated for with a longer interaction length (5 times longer for the shown example).

In addition to coupling to higher order waveguide mode families, one can also identify a rising background in the high velocity region. It can be attributed to strong coupling to the substrate modes in the Cherenkov regime ($v \gtrsim 0.7c$), where the charged particle velocity exceeds the phase velocity of light in dielectric media (silica). In Appendix A, we show that we can isolate the contribution of the substrate bulk modes. This contribution can be suppressed by either choosing an electron velocity well below the Cherenkov regime of the substrate, or by using a low index material as the substrate (e.g. by suspending the structure in air).

We can now quantitatively evaluate the coupling ideality to the TM_{00} mode as a function of electron velocity, shown in Fig.4(a-b). Some applications require electron energy filtering; for example a heralded single pho-

ton source can be realized by conditioning on the first photon-energy loss sideband in the electron energy measurement record. We assume an electron energy resolution of 0.5 eV with Gaussian zero-loss-peak (ZLP) profile, and show that one can easily achieve more than 99 % sideband filtered coupling ideality I^* to the TM_{00} mode outside the Cherenkov regime ($v_e \lesssim 0.7c$) with a single mode waveguide and the electron beam positioned $\gtrsim 100$ nm above the surface. The sideband filtering will eventually be limited by the residual broadband coupling to the unguided bulk modes of the substrate. For applications that are sensitive to the full optical spectrum, we show that more than 90 % coupling ideality I can be achieved with the electron beam placed $\gtrsim 300$ nm above the surface, mostly limited by the parasitic coupling to the higher order waveguide modes. One can always place the electron beam further away from the waveguide surface to achieve higher ideality, at the expense of reduced coupling strength. This trade-off is illustrated in Fig.4(c), where the total coupling strength $|g_{\mathrm{TM}_{00}}|^2$ is plotted against the coupling idealities. However, a reduced coupling strength due to a larger electron-surface gap can always be compensated with longer interaction length. As a result, given a fixed waveguide geometry and a target total coupling strength, the minimum deviation from ideality of unity is inversely proportional to the interaction length.

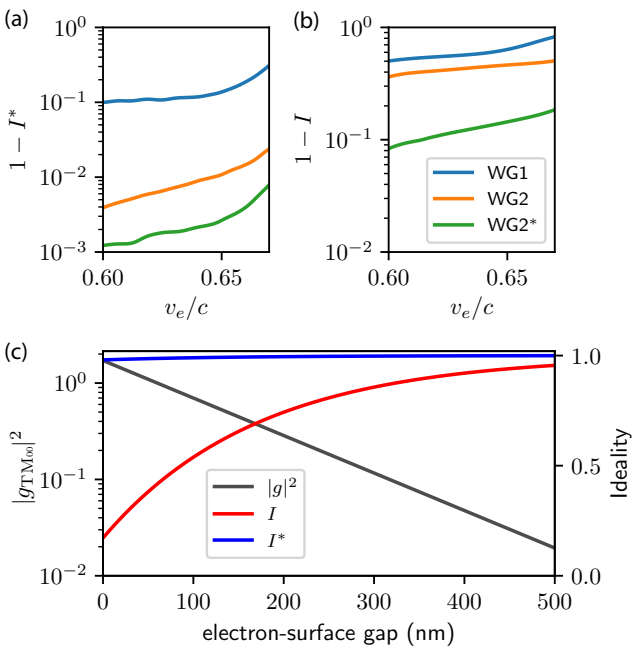

FIG. 4. Coupling ideality deviation from unity with **(a)** sideband filtering ($1 - I^*$) and **(b)** no filtering ($1 - I$), shown with different waveguide/electron configurations (WG1:2.1 μm width; WG2:800 nm width; WG2*:electron beam 200nm further away from the waveguide surface), as a function of electron velocity. **(c)** Total coupling strength of TM_{00} mode vs coupling idealities as a function of gap distance between the electron beam and the waveguide surface, with 800 nm waveguide width, 100 μm interaction length and $v_e/c = 0.65$ electron velocity.

IV. DISCUSSION

We have analyzed the coupling of free electrons to photonic integrated circuits. Our results show that by controlling electron velocity, electron beam positioning and waveguide design, the parasitic coupling contributions can be efficiently suppressed, which results in near-unity coupling ideality to the target TM_{00} mode of the waveguide in the studied example. In the special cases where the waveguide loops and forms a resonator, the same treatment can be applied, and the open ended waveguide result can also be easily extended to treat the resonator case (see Appendix G).

In addition to the near-unity coupling ideality achievable with photonic integrated waveguides, the platform offers versatile optical waveform shaping and frequency tuning. The spatial-temporal optical mode $\hat{a}_m$ defined by the electron-photon interaction has a spatial-temporal profile $\phi_m(\mathbf{r}, t)$ along the waveguide direction which can be expressed as

$$\phi_m(\mathbf{r}, t) \propto \int dz K(z, \mathbf{r}, t) \overline{U}^*_{m,z}(\mathbf{R_0}, z, \omega_m) e^{-i\omega_m t},$$

which connects $\phi_m(\mathbf{r}, t)$ to the envelope of the optical mode profile $U_{m,z}(\mathbf{R_0}, z, \omega_m)$ along the electron propagation trajectory through an integral kernel $K(z, \mathbf{r}, t)$ (for details see Appendix F). The integral kernel depends on the waveguide dispersion, and behaves asymptotically as the Dirac delta function in the weak dispersion limit. In such a limit, the spatial-temporal profile conforms to the shape of the optical mode envelope over the electron trajectory. Since the electron travels in a straight path in the no-recoil limit, by using a tailor-made waveguide structure with proper dispersion and routing, most types of waveforms of the optical state can be achieved. The center frequency of the optical excitation can also be easily tuned by selecting the appropriate electron velocity, evident in the results shown in Fig.3. These features of the interacting optical modes promise potential application as a tunable single photon source, and are crucial for realizing entanglement protocols with other quantum systems through optical links, by matching the optical frequency and waveform to the target quantum system.

Our analysis and results indicate that the photonic integrated waveguide platform is an ideal environment for free-electron quantum optics, which promises a pathway to high-fidelity photon state synthesis, heralded single-electrons, entanglement of free electrons with other quantum systems and quantum-enhanced sensing and imaging.

ACKNOWLEDGMENTS

This work was supported by the Swiss National Science Foundation under grant agreement 185870 (Ambizione). O.K. gratefully acknowledges the Young Faculty Award from the National Quantum Science and Technology program of the Israeli Planning and Budgeting Committee.

Appendix A: Substrate and thin film losses

We have discussed in the main text the different scaling of $\Gamma(\omega)$ for bulk substrate, thin film, and guided modes. We show their electron energy loss characteristics in Fig.A.1 with an electron 100 nm above the dielectric surface. It is shown that for a given frequency component ω, the quadratic scaling of a guided mode will dominate the interaction. However, for a waveguide structure with linear dispersion (e.g. the one shown in Fig.A.1(a)), the phase matching condition will enforce a linear scaling of the total deposited quanta into one particular waveguide mode. But due to relatively weak dispersion of the waveguide modes, the coupling contribution from the waveguide modes dominates over substrate losses, where the latter accounts for less than 2% of the total coupling strength over a 0.5 eV band with electron velocity $v_e/c \leq 0.6$. For unpatterned thin film, the total photon emission is 70% lower than for a waveguide, but the emission is less structured and hard to collect. Note that due to the presence of waveguide dispersion, the coupling strengths are linearly dependent on distance. Therefore, the ratio of different coupling contributions is distance independent, and only depends on waveguide dispersion and routing, and e-beam positioning.

Appendix B: QED details

We consider an electron beam with a narrow momentum spread around wavevector $\mathbf{k}_0$ and assume that the photon energies involved in the interaction are much smaller than the electron relativistic energy $E_0 = c\sqrt{c^2m^2 + \hbar^2 k_0^2}$ (i.e. the no-recoil regime). In the velocity gauge, the Hamiltonian is described as [49, 50]

$$\hat{H} = \hat{H}_{\rm el} + \hat{H}_{\rm ph} + \hat{H}_{\rm int}$$
$$\hat{H}_{\rm el} = \sum_{\mathbf{k}} [E_0 + \hbar \mathbf{v}\cdot(\mathbf{k}-\mathbf{k}_0)]\hat{c}^\dagger_{\mathbf{k}}\hat{c}_{\mathbf{k}}$$
$$\hat{H}_{\rm ph} = \int d\omega \int d^3\mathbf{r}\hbar\omega \hat{\mathbf{f}}^\dagger(\mathbf{r},\omega)\cdot\hat{\mathbf{f}}(\mathbf{r},\omega)$$
$$\hat{H}_{\rm int} = -\int d^3\mathbf{r}\hat{\mathbf{J}}(\mathbf{r})\cdot\hat{\mathbf{A}}(\mathbf{r})$$

where we defined the electron current operator $\hat{\mathbf{J}}(\mathbf{r}) = (-e\mathbf{v}/V)\sum_{\mathbf{k},\mathbf{q}} e^{i\mathbf{q}\cdot\mathbf{r}}\hat{c}^\dagger_{\mathbf{k}}\hat{c}_{\mathbf{k}+\mathbf{q}}$ using the Fermionic ladder operators $\hat{c}_{\mathbf{k}}$ and the relativistic electron group velocity $\mathbf{v} = \hbar c^2\mathbf{k}_0/E_0$. The vector potential $\hat{\mathbf{A}}(\mathbf{r},t) = \int \frac{d\omega}{2\pi}\hat{\mathbf{A}}(\mathbf{r},\omega)e^{i\omega t} + h.c.$ is associated with the noise current operator $\hat{\mathbf{j}}^{\rm noise}(\mathbf{r},\omega)$ through the quantized three-dimensional Maxwell equation[46] and has a formal solution

$$\hat{\mathbf{A}}(\mathbf{r},\omega) = -4\pi\int d^3\mathbf{r}' G(\mathbf{r},\mathbf{r}',\omega)\cdot\hat{\mathbf{j}}^{\rm noise}(\mathbf{r}',\omega)$$

where $G(\mathbf{r},\mathbf{r}',\omega)$ is the dyadic Green function (Green tensor) of the classical problem satisfying the equation

$$\nabla\times\nabla\times G(\mathbf{r},\mathbf{r}',\omega) - \frac{\omega^2}{c^2}\epsilon(\mathbf{r},\omega)G(\mathbf{r},\mathbf{r}',\omega) = -\mu_0\delta(\mathbf{r}-\mathbf{r}')$$

which describes the field response at $\mathbf{r}$ to a point current excitation at $\mathbf{r}'$. Since we are dealing with non-magnetic materials, we assume a relative permeability $\mu(\mathbf{r}) = 1$. The noise operator is bosonic and was chosen to be

$$\hat{\mathbf{j}}^{\rm noise}(\mathbf{r},\omega) = \omega\sqrt{\hbar\epsilon_0 {\rm Im}\{\epsilon(\mathbf{r},\omega)\}}\hat{\mathbf{f}}(\mathbf{r},\omega)$$

in order to satisfy the fluctuation-dissipation theorem due to dissipative material, with bosonic ladder operators $\hat{\mathbf{f}}(\mathbf{r},\omega)$ satisfying commutation relation $\left[\hat{f}_i(\mathbf{r},\omega), \hat{f}'_i(\mathbf{r}',\omega')\right] = \delta_{i,i'}\delta(\mathbf{r}-\mathbf{r}')\delta(\omega-\omega')$. Note that in the limiting case of a dispersive material (assumed in this study, characterized by its instantaneous electronic response) ${\rm Im}\{\epsilon(\mathbf{r},\omega)\} \to 0$, the formalism imposes no problem and is shown to correctly reduce to mode decomposition method used in the quantized vacuum field[51] due to Kramers–Kronig relations.

When projecting to the direction of the electron trajectory $\hat{\mathbf{z}}$ with transverse coordinate $\mathbf{R}_0$, the scattering matrix is shown to be

$$\hat{S} = e^{i\hat{\chi}}\hat{U}$$
$$\hat{U} = \exp\left\{\left[\frac{-ie}{2\pi\hbar V^{2/3}}\sum_{\mathbf{k},\mathbf{q}_\perp}\int d\omega\int d^3\mathbf{r}e^{i\mathbf{q}_\perp\cdot\mathbf{R}}e^{-i\omega z/v}\right.\right.$$
$$\left.\left.\hat{A}_z(\mathbf{r},\omega)\hat{c}^\dagger_{\mathbf{k}}\hat{c}_{\mathbf{k}+\mathbf{q}_\perp-(\omega/v)\hat{\mathbf{z}}}\right] - h.c.\right\}$$

where $\mathbf{q}_\perp$ is the transverse component of the exchanged electron wave vector. We can further simplify the expression by disregarding the phase operator $\hat{\chi}$ and average over the transverse electron state, and obtain

$$\hat{U} = \exp\left[\int d\omega g_\omega \hat{b}^\dagger_\omega\hat{a}_\omega - h.c.\right]$$

where traveling photon and electron operators are introduced

$$\hat{a}_\omega = -\frac{ie}{2\pi\hbar g_\omega}\int dz e^{-i\omega z/v}\hat{A}_z(\mathbf{R}_0,z,\omega)$$
$$\hat{b}_\omega = \sum_{k_z}\hat{c}^\dagger_{k_z}\hat{c}_{k_z+\omega/v}$$

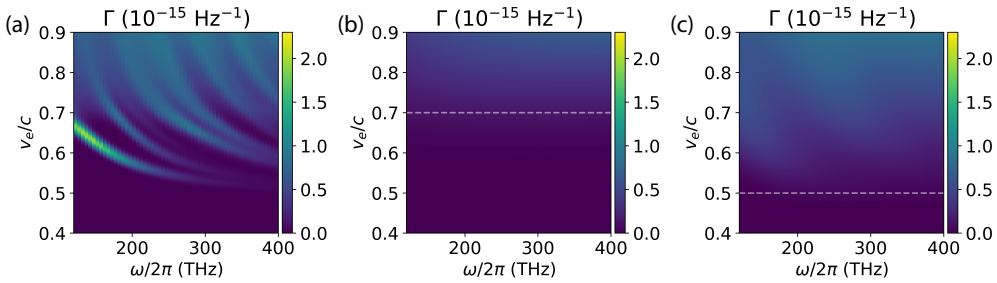

FIG. A.1. Electron energy loss spectrum for a 50 μm interaction distance with **(a)** waveguides, **(b)** silica substrate, and **(c)** Si_3N_4thin film on silica substrate. Notice that for a waveguide the scaling is quadratic with respect to distance and more structured, whereas for substrate and thin film the scaling is mostly linear and the emission is more broadband. The interaction with the waveguide mode will prevail over substrate and thin film over an interaction length of just a few wavelengths. The dashed gray lines are a guide to the eye showing Cherenkov regime boundaries for silica and Si_3N_4.

with vacuum coupling strength g_ω associated with the electron energy loss (EELS) probability studied in this manuscript

$$|g_\omega|^2 = \Gamma(\mathbf{R}_0,\omega) = \frac{4e^2}{\hbar}\iint dz dz' \mathrm{Re}\{ie^{i\omega(z-z')/v}G_{zz}(\mathbf{R}_0,z;\mathbf{R}_0,z';\omega)\}.$$

The operators are defined in this way so that the quantum optical commutation relations are preserved $[\hat{a}_\omega,\hat{a}^\dagger_{\omega'}] = \delta(\omega-\omega')$, and can be easily proven using the identity

$$\sum_{i''}\int d^3\mathbf{r}''\mathrm{Im}\{\epsilon(\mathbf{r}'',\omega)\}G_{i,i''}(\mathbf{r},\mathbf{r}'',\omega)G^*_{i',i''}(\mathbf{r}',\mathbf{r}'',\omega) = -\frac{1}{\epsilon_0\omega^2}\mathrm{Im}\{G_{i,i'}(\mathbf{r},\mathbf{r}',\omega)\}.$$

Note that $\hat{a}_\omega$ contains contributions from all the spatial modes at ω, and is not defined for a specific spatial mode $\hat{a}_{\omega,m}$ which is frequently used in cavity QED systems. It is in this way advantageous to use this formalism to account for the infinite number of spatial modes the electron couples to. If the transverse spread is significant, the EELS probability is shown [52] to be an average over the transverse electron wavefunction

$$\Gamma(\omega) = \int d^2\mathbf{R}|\psi_\perp(\mathbf{R})|^2\Gamma(\mathbf{R},\omega)$$

Appendix C: Equivalence to classical result

The electron energy loss at a dielectric surface can be interpreted classically in a microscopic picture [53], see Fig.1: if an electron passes near the surface of a dielectric structure, the dipoles in the structures are polarized, induced by the electric field from the flying electron, and generates a backaction field $\mathbf{E}(\mathbf{r}_e(t),t)$ to the electron at $\mathbf{r}_e(t)$ that induces electron energy loss. The total energy loss can be expressed in time domain and frequency domain as

$$\Delta E = e\int dt\mathbf{v}\cdot\mathbf{E}(\mathbf{r}_e(t),t) = \int \hbar\omega d\omega\Gamma(\omega)$$

where the frequency domain energy loss function $\Gamma(\omega)$ is expressed as

$$\Gamma(\omega) = \frac{e}{\pi\hbar\omega}\int dt\mathrm{Re}\left[e^{-i\omega t}\mathbf{v}\cdot\mathbf{E}(\mathbf{r}_e(t),\omega)\right]$$

which can be verified easily if one plugs it back into the energy loss expression and the correct time integral is retrieved. Notice that here $\mathbf{E}(\mathbf{r}_e(t),\omega)$ is not the direct Fourier transform of $\mathbf{E}(\mathbf{r}_e(t),t)$, but only on the time dependence of the electric field function not explicitly depending on the electron trajectory function $\mathbf{r}_e(t)$. The frequency domain components depends explicitly on the current induced from a given electron trajectory, but do not take into account the sampling of the field at different position $\mathbf{r}_e(t)$ at different time t. This ensures that the total energy loss is consistent, but renders the formalism non-local. This treatment is consistent with the quantum formalism when the electron is decomposed into perfect momentum states where the wavepacket length is infinite, as one could see from the fact that even though electron only interacts with the structure locally, the resulting energy loss spectrum will show e.g. discrete mode structure (a non-local property). This is the result of this particular Fourier expansion procedure, but when considering the electron in terms of wave packets this treatment is valid. It has been shown [52] that a full quantum treatment gives exactly the same EELS result.

Using the no-recoil approximation, which assumes that the radiation of electron into the surrounding substrates does not change the trajectory $\mathbf{r}_e(t)$ of the electron significantly, we can directly calculate the induced electric field $\mathbf{E}(\mathbf{r}_e(t),t)$ from the electron current $\mathbf{j}(\mathbf{r},t)$ through the Green tensor of the whole dielectric structure,

$$\mathbf{E}(\mathbf{r},\omega) = -4\pi i\omega\int d^3\mathbf{r}'G(\mathbf{r},\mathbf{r}',\omega)\cdot\mathbf{j}(\mathbf{r}',\omega)$$

where the Green tensor $G(\mathbf{r},\mathbf{r}',\omega)$ is the elementary solution of the full Maxwell equation

$$\nabla\times\nabla\times G(\mathbf{r},\mathbf{r}',\omega)-\frac{\omega^2}{c^2}\epsilon(\mathbf{r},\omega)G(\mathbf{r},\mathbf{r}',\omega)=-\mu_0\delta(\mathbf{r}-\mathbf{r}')$$

with a point current at position $\mathbf{r}'$ in frequency domain. A flying electron is equivalent to a broadband evanescent source, and here we consider an electron beam at $\hat{\mathbf{z}}$ direction at transverse coordinate $\mathbf{R}_0$, for which the frequency domain electron current density is

$$\mathbf{j}(\mathbf{r},\omega)=-e\hat{\mathbf{z}}\delta(\mathbf{R}-\mathbf{R}_0)e^{i\omega(z-z_0)/v}.$$

From here, one can express the frequency domain loss rate in terms of Green function as

$$\Gamma(\omega)=\frac{4e^2}{\hbar}\int dzdz'\mathrm{Re}[ie^{i\frac{\omega(z-z')}{v}}G_{zz}(\mathbf{R}_0,z;\mathbf{R}_0,z';\omega)],$$

which coincides with the result from a full QED treatment. One should keep in mind that the Green tensor here has two contributions, one from vacuum G_0 and the other from the backaction field G_{ind} from the induced dielectric dipoles. Only the backaction field G_{ind} contributes to electron energy loss, because electron does not emit in vacuum so the contribution from the vacuum G_0 vanishes in the integral.

Appendix D: Correspondence to modal decomposition

The correspondence between the 3D macroscopic quantization method in dispersive material with the conventional quantum optics quantization procedure using modal decomposition has been demonstrated for the 1D case [51]. Here, we show the correspondence with the quantum optical formalism used in [29]. To account for all the spatial modes at a given frequency ω, the quantization of vector potential was chosen as

$$\hat{\mathbf{A}}(\mathbf{r},\omega)=-4\pi\omega\int d^3\mathbf{r}'\sqrt{\hbar\epsilon_0\mathrm{Im}\{\epsilon(\mathbf{r}',\omega)\}}G(\mathbf{r},\mathbf{r}',\omega)\cdot\hat{\mathbf{f}}(\mathbf{r}',\omega)$$

to fulfill the canonical field commutation relations. However, in vacuum or lossless media, the modal decomposition method [54] is often used instead, with

$$\hat{\mathbf{A}}(\mathbf{r},t)=\sum_m\sqrt{\frac{\hbar}{2\omega_m\epsilon_0}}\mathbf{U}_m(\mathbf{r})\hat{a}_{\omega_m,m}e^{-i\omega_m t}+h.c.$$

where the profile function $\mathbf{U}_m(\mathbf{r})$ of each mode defined in a frequency window $\Delta\omega_m$ satisfies the wave equation

$$\nabla\times\nabla\times\mathbf{U}_m(\mathbf{r})-\frac{\omega^2}{c^2}\epsilon(\mathbf{r},\omega_m)\mathbf{U}_m(\mathbf{r})=0$$

with normalization condition

$$\int d^3\mathbf{r}\epsilon(\mathbf{r},\omega_m)\mathbf{U}_m(\mathbf{r})\cdot\mathbf{U}_n^*(\mathbf{r})=\delta_{m,n}.$$

From here, one can easily find the correspondence between the spatial mode ladder operators $\hat{a}_{\omega,m}$ and the bosonic ladder operators $\hat{\mathbf{f}}(\mathbf{r}',\omega)$ as

$$\hat{a}_{\omega_m,m}=-4\pi\int_{\Delta\omega_m}d\omega\iint d^3\mathbf{r}d^3\mathbf{r}'$$
$$\sqrt{2\omega^2\omega_m\mathrm{Im}\{\epsilon(\mathbf{r}',\omega)\}}\epsilon_0\epsilon(\mathbf{r},\omega)\mathbf{U}_m^*(\mathbf{r})\cdot G(\mathbf{r},\mathbf{r}',\omega)\cdot\hat{\mathbf{f}}(\mathbf{r}',\omega),$$

with their vacuum coupling strength to the electron as [39]

$$g_{\omega_m,m}(\mathbf{R}_0)=\sqrt{\frac{e^2}{2\epsilon_0\hbar\omega_m}}\int dze^{-i\omega_m z/v}U_{m,z}(\mathbf{R}_0,z).$$

In this formalism, we can rewrite the scattering matrix in its modal decomposition form

$$\hat{S}=e^{i\hat{\chi}}\exp\left[\int d\omega g_\omega\hat{b}_\omega^\dagger\hat{a}_\omega-h.c.\right]$$
$$=e^{i\hat{\chi}'}\exp\left[\sum_m g_{\omega_m,m}\hat{b}_{\omega_m}^\dagger\hat{a}_{\omega_m,m}-h.c.\right]$$

where the optical mode operators $\hat{a}_{\omega_m,m}$ are no longer traveling mode operators and now satisfy $[\hat{a}_{\omega_m,m},\hat{a}_{\omega_n,n}^\dagger]=\delta_{m,n}$.

In the case of an optical cavity, the optical modes are well-defined bosonic modes. As long as the electron energy resolution does not resolve frequency structure of the optical mode, the treatment is valid. For an open waveguide, the modes that are coupled to the electron are instead travelling modes in a continuum [55]. The vacuum coupling strength of a continuum frequency mode in a spatial mode family is

$$g_{\omega,m}(\mathbf{R}_0)=\sqrt{\frac{e^2}{2\epsilon_0\hbar\omega}}\int dze^{-i\omega z/v}\tilde{U}_{m,z}(\mathbf{R}_0,z,\omega),$$

where the profile function $\tilde{\mathbf{U}}_m(\mathbf{r},\omega)$ satisfies the wave equation as well, but with normalization condition

$$\int d^3\mathbf{r}\epsilon(\mathbf{r},\omega)\tilde{\mathbf{U}}_m(\mathbf{r},\omega)\cdot\tilde{\mathbf{U}}_n^*(\mathbf{r},\omega')=\delta_{m,n}\delta(\omega,\omega').$$

Index m here represents different spatial mode families. However, when the electron energy resolution does not resolve the frequency structure of the coupling strength to any given mode family, one can still define the corresponding non-continuous operators for different mode families,

$$\hat{a}_m=\int d\omega\phi_m^*(\omega)\hat{a}_\omega$$
$$\hat{a}_\omega=\sum_m\phi_m(\omega)\hat{a}_m$$

where $\phi_m(\omega)$ is the Fourier component of the temporal field profile functions [56, 57]

$$\phi_m(\mathbf{r},t) = i\int d\omega \sqrt{\frac{\hbar\omega}{2\epsilon_0}}\phi_m(\omega)\tilde{\mathbf{U}}_m(\mathbf{r},\omega)e^{-i\omega t}$$
$$\hat{E}(\mathbf{r},t) = \sum_m \phi_m(\mathbf{r},t)\hat{a}_m + h.c.$$

of the defined mode families. It is a complete orthogonal set of functions on ω,

$$\int d\omega \phi_m(\omega)\phi_n^*(\omega) = \delta_{m,n}$$
$$\sum_m \phi_m(\omega)\phi_m^*(\omega') = \delta(\omega-\omega')$$

found through Gramm-Schmit orthonormalization procedure, such that the commutation relation $[\hat{a}_m, \hat{a}_n^\dagger] = \delta_{m,n}$ is satisfied for these so called *field operators* in the context of quantum field theory, introduced to avoid using operator-valued distributions. One can therefore rewrite the scattering matrix in the new mode family field operator basis

$$\hat{S} = e^{i\hat{\chi}}\exp\left[\sum_m g_m \hat{b}_m^\dagger \hat{a}_m - h.c.\right]$$

where $g_m = \int d\omega g_\omega \phi_m(\omega)$. The total coupling strength would be $|g_m|^2 = \iint d\omega d\omega' g_\omega g_{\omega'}^* \phi_m(\omega)\phi_m^*(\omega')$. Here, when the frequency bands of different mode families with non-negligible coupling strength g_ω are sufficiently separated, we choose the profile function $\phi_m(\omega) = \mathbb{I}_{\omega\in\Delta\omega_m} g_\omega^*/g_m^*$, where $\Delta\omega_m$ is the frequency window within which we define the field operator for the corresponding mode family, and $|g_m|^2 = \int_{\Delta\omega_m} d\omega |g_\omega|^2$. Note that when the coupling to bulk modes is significant, one has to use the coupling strength $g_{\omega,m}$ from the conventional modal decomposition method instead of the Green function method to quantitatively isolate the coupling to a mode family from background bulk mode contributions.

The cavity mode decomposition is actually the narrowband approximation of the Gramm-Schmit orthonormalization procedure, where $\phi_m(\omega)$ is strongly peaked around the mode center frequency, since all optical modes, though narrow, still have a finite linewidth due to the coupling to outside channels (e.g. bus waveguide). The profile function can be found through the input-output formalism [58] of an optical cavity $\hat{a}_m$, assuming unity coupling efficiency to the bus waveguide mode $\hat{a}_{\text{out}}$ with coupling rate κ, which results in a profile function of $\phi_m(\omega) \propto \frac{\sqrt{\kappa}}{-\frac{\kappa}{2}+i(\omega_m-\omega)}$, where the bus waveguide is part of the resonator and forms the continuum modes in frequency domain.

Appendix E: COMSOL simulation details

The Green tensor solution of Maxwell equation is not directly supported in COMSOL, but can be retrieved by Frequency domain study with the RF module. The waveguide is an air cladded Si_3N_4slab embedded in SiO2 substrate with different geometries mentioned in the main text. Perfect matching layers at boundaries are used to prevent boundary reflections and in turn allow us to simulate an infinitely long waveguide. In order to solve for the Green function $G(\mathbf{r},\mathbf{r}',\omega)$, a point oscillating electric current dipole $\mathbf{J}(\omega) = \mathbf{p}(\omega)\delta(\mathbf{r}-\mathbf{r}_0)$ is placed 100 nm (or 300 nm) above the waveguide surface at position $\mathbf{r}_0$. COMSOL solves for the electric field which relates to the Green tensor as

$$\mathbf{E}(\mathbf{r},\omega) = -4\pi i\omega G(\mathbf{r},\mathbf{r}_0,\omega)\cdot\mathbf{p}(\omega)$$

and thus if one wishes to retrieve G_{zz} component one needs to orient the electric dipole $\mathbf{p} = p\hat{\mathbf{z}}$ along the z direction $\hat{\mathbf{z}}$, and look at the electric field z component E_z, such that

$$G_{zz}(\mathbf{r},\mathbf{r}',\omega) = \frac{E_z(\mathbf{r},\omega)}{-4\pi i\omega p(\mathbf{r}',\omega)}$$

The results are illustrated in Fig.2. The Green function can be thought of as the spatial pattern of electron emission in the waveguide (or surrounding substrates), and thus their spatial pattern at different optical frequency ω relates to the excited optical modes given the right electron velocity (only if the field provides backaction force to the electron, otherwise in free space electron does not emit light). The Green function along the electron trajectory is shown in Fig.E.1(a), where one can clearly see the bulk mode contribution near the dipole position,

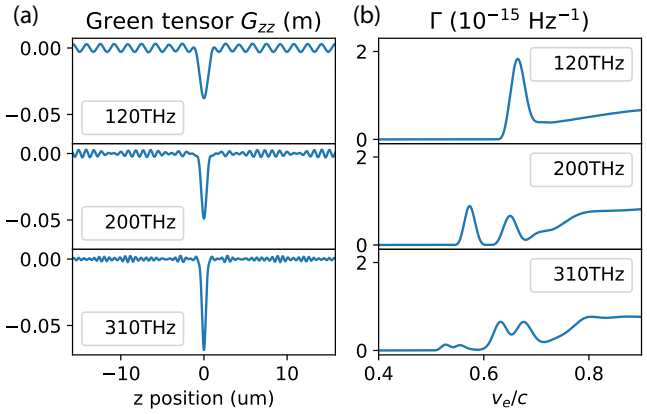

FIG. E.1. **(a)** Examples of the Green function $\text{Im}[G_{zz}(\mathbf{r},\mathbf{r}_0,\omega)]$ along the trajectory of the electron at different optical frequencies, and **(b)** the corresponding vacuum coupling strength at different electron velocities, for a 50 μm interaction length. The spatial beating of many mode families is visible in the Green functions, and also in the coupling strength. The coupling to different mode families is phase matched at different electron velocities at a given optical frequency. When the electron velocity is in the Cherenkov regime ($v \gtrsim 0.7c$), the energy loss is eventually dominated by the substrate loss.

and spatial beatings of different waveguide modes under some conditions. The total coupling strength is related to the Green function through a spatial Fourier transform, and shown in Fig.E.1(b), where one can identify several prominent peaks, mainly contributed from the waveguide modes, and a rising background in the Cherenkov regime ($v \gtrsim 0.7c$) of the silica substrate due to the enhanced bulk mode coupling. The Blackman window is used to eliminate the ripples from Fourier transform due to finite simulation length. The center velocity of the peaks corresponds to the optical mode phase velocity, and the bandwidth is determined by the interaction length (in this case set to $50\,\mu$m). By sweeping the optical frequency in the simulation across the range where we have access to material permittivity, one retrieves the 2D map shown in Fig.3.

Appendix F: Quantum state from the electron-photon interaction

The composite quantum state after the electron-photon interaction is

$$\begin{aligned}|\psi\rangle &= \exp\left(\int d\omega g_\omega \hat{b}_\omega^\dagger \hat{a}_\omega - h.c.\right)|\psi_e\rangle|0\rangle \\ &= e^{-\frac{\int d\omega |g_\omega|^2}{2}} e^{-\int d\omega g_\omega^* \hat{b}_\omega \hat{a}_\omega^\dagger} e^{\int d\omega g_\omega \hat{b}_\omega^\dagger \hat{a}_\omega}|\psi_e\rangle|0\rangle \\ &= e^{-\frac{\int d\omega |g_\omega|^2}{2}} e^{-\int d\omega g_\omega^* \hat{b}_\omega \hat{a}_\omega^\dagger}|\psi_e\rangle|0\rangle \\ &= e^{-\frac{\int d\omega |g_\omega|^2}{2}} \sum_n \frac{\left(-\int d\omega g_\omega^* \hat{b}_\omega \hat{a}_\omega^\dagger\right)^n}{n!}|\psi_e\rangle|0\rangle\end{aligned}$$

when conditioned on the nth energy sideband of the electron state (with electron ZLP much wider than the coupling bandwidth to the optical modes), the optical state collapses to

$$|\psi_o\rangle \sim \left(-\int d\omega g_\omega^* \hat{a}_\omega^\dagger\right)^n |0\rangle$$

and when the interaction is dominated by coupling to a single optical mode family, one can generate single mode Fock state in a probabilistic way

$$\begin{aligned}|\psi_o\rangle &\sim \left(\hat{a}_m^\dagger\right)^n |0\rangle \\ \hat{a}_m &= \int_{\Delta\omega_m} d\omega \phi_m(\omega)\hat{a}_\omega \\ \phi_m(\omega) &= \frac{g_{\omega,m}^*}{g_m^*}\end{aligned}$$

From these result, one quantity that one might be interested in is the temporal field profile function generated by this interaction, as it may concern many experiments that require waveform overlap. Straight from the definition, one gets

$$\phi_m(\mathbf{r},t) \propto \iint dz d\omega e^{i\omega(z/v-t)} \tilde{U}_{m,z}^*(\mathbf{R}_0,z,\omega)\tilde{\mathbf{U}}_m(\mathbf{r},\omega)$$

One can further remove the frequency dependence of the mode profile functions by assuming an open waveguide (e.g. no sharp frequency response in the phase matched region) and up to second order dispersion β,

$$\tilde{\mathbf{U}}_m(\mathbf{r},\omega) \approx \tilde{\mathbf{U}}_m(\mathbf{r},\omega_m) e^{i(\omega-\omega_m)r_\parallel/v_g} e^{i\beta(\omega-\omega_m)^2 r_\parallel/v_g},$$

where ω_m is the center frequency of the pulse, selected so that the phase velocity at ω_m matches the electron velocity v, $v_g \lesssim v$ is the corresponding group velocity, and $r_\parallel$ is the longitudinal coordinate along the waveguide trajectory. One can then rewrite the expression as

$$\begin{aligned}\phi_m(\mathbf{r},t) &\propto \iint dz d\omega e^{i\frac{(\omega-\omega_m)}{v}(z-\frac{v}{v_g}(R_\parallel(z)-r_\parallel)-vt)} \\ &e^{i\beta\frac{(\omega-\omega_m)^2}{v_g}(r_\parallel-R_\parallel(z))} e^{i\omega_m(z/v-t)} \tilde{U}_{m,z}^*(\mathbf{R}_0,z,\omega_m)\tilde{\mathbf{U}}_m(\mathbf{r},\omega_m) \\ &\propto \int dz e^{i\frac{\left(z-\frac{v}{v_g}(R_\parallel(z)-\tilde{r}_\parallel)\right)^2}{4\beta(r_\parallel-R_\parallel(z))v^2/v_g}} \frac{e^{i\frac{\pi}{4}\mathrm{sgn}(\beta(r_\parallel-R_\parallel(z)))}}{\sqrt{|\beta(r_\parallel-R_\parallel(z))|}} \\ &e^{i\omega_m(z/v-t)} \tilde{U}_{m,z}^*(\mathbf{R}_0,z,\omega_m)\tilde{\mathbf{U}}_m(\mathbf{r},\omega_m) \\ &\propto \int dz K(z,\mathbf{r},t) \overline{\tilde{U}}_{m,z}^*(\mathbf{R}_0,z,\omega_m)\tilde{\mathbf{U}}_m(\mathbf{r},\omega_m)e^{-i\omega_m t}\end{aligned}$$

$\tilde{r}_\parallel \equiv r_\parallel - v_g t$ is the waveform coordinate in the pulse frame, where the phase-zero point is traveling at the waveguide group velocity v_g. $\overline{\tilde{U}}_{m,z}^*(\mathbf{R}_0,z,\omega_m)$ is the mode envelope profile at wave vector ω_m/v. The integral kernel

$$K(z,\mathbf{r},t) \equiv e^{i\frac{\left(z-\frac{v}{v_g}(R_\parallel(z)-\tilde{r}_\parallel)\right)^2}{4\beta(r_\parallel-R_\parallel(z))v^2/v_g}} \frac{e^{i\frac{\pi}{4}\mathrm{sgn}(\beta(r_\parallel-R_\parallel(z)))}}{\sqrt{|\beta(r_\parallel-R_\parallel(z))|}}$$

is a phase scrambling around waveform coordinate $\tilde{r}_\parallel$ with a bandwidth of $\sim |\beta(r_\parallel)v^2/v_g|$, due to the presence of second order dispersion. One can get a physical intuition of the waveform in the limit of weak dispersion ($\beta \to 0$), where one can approximate the integral kernel with a Dirac delta function,

$$\begin{aligned}\phi_m(\mathbf{r},t) &\propto \int dz \delta(z-\frac{v}{v_g}(R_\parallel(z)-\tilde{r}_\parallel)) \\ &\overline{\tilde{U}}_{m,z}^*(\mathbf{R}_0,z,\omega_m)\tilde{\mathbf{U}}_m(\mathbf{r},\omega_m)e^{-i\omega_m t} \\ &\propto \sum_i \frac{\overline{\tilde{U}}_{m,z}^*(\mathbf{R}_0,z_i,\omega_m)}{|R_{\parallel\partial z}(z_i)-\frac{v_g}{v}|}\tilde{\mathbf{U}}_m(\mathbf{r},\omega_m)e^{-i\omega_m t}\end{aligned}$$

where $z_i(\mathbf{r},t)$: $\frac{z_i}{v} - \frac{1}{v_g}(R_\parallel(z_i)-\tilde{r}_\parallel) = 0$ are the spatial z coordinates where the vacuum field contributes the most through the phase-matching condition to the generated field at $\mathbf{r}$ coordinate at time t. Therefore, the excited optical profile in the time domain is easily connected to the envelope of the optical mode field profile $\tilde{U}_{m,z}(\mathbf{R}_0,z,\omega_m)$ along the electron propagation direction, when the mode dispersion is sufficiently weak. In the exact limit $\beta = 0$, there can be unphysical scenarios when

$|R_{\|\partial z}(z_i) - \frac{v_g}{v}| = 0$, which corresponds to the infinite phase matching bandwidth. However, in physical materials, the phase matching bandwidth is always finite.

The mode dispersion during pulse propagation will cause pulse shortening or broadening by shifting the phase of different frequency components and leaving the amplitude unchanged. This can be easily corrected and is not a fundamental limit to construct an arbitrary waveform. Therefore, one can structure any desired optical waveform $\phi(\mathbf{r}, t)$ by positioning the electron beam trajectory on an optical waveguide with a tailor-made waveguide structure.

Appendix G: Interaction with optical resonators

We only discussed results for open ended waveguides so far. However, there have been experiments [29, 39] that uses optical resonators with a discrete set of well-defined frequency modes instead of a continuum of frequency modes in the case of a waveguide. These well-defined modes in state of the art resonators typically have optical linewidths of tens of MHz [41], and it is therefore difficult to resolve their Green functions by sweeping the optical frequencies in FEM simulations. Nonetheless, their Green functions can be easily related to the one of open ended optical waveguides by their optical susceptibility function $\chi(\omega) = \frac{2}{\pi}\frac{\mathcal{F}}{1+4(\omega-\omega_0)^2/\kappa^2}$ enforced by the resonator periodic boundary conditions, describing an optical resonance with center frequency ω and Finesse $\mathcal{F} = \frac{\Delta\nu_{\mathrm{FSR}}}{\kappa}$. One can retrieve the resonator Green function $G(\omega)$ by separating the open waveguide Green function into contributions from different cavity modes (with mode field function $\mathbf{U}_m(\mathbf{r})$, details see Appendix D)

$$G_m(\mathbf{r}, \mathbf{r}', \omega) = \mathbf{U}_m(\mathbf{r}') \int d^3\mathbf{r}'' \epsilon(\mathbf{r}'', \omega) \mathbf{U}_m^*(\mathbf{r}'') G(\mathbf{r}, \mathbf{r}'', \omega),$$

and multiplying the resonance susceptibilities $G(\omega) = \sum_m G_m(\omega) \sum_m \chi_m(\omega)$. For a closed loop resonator structure, the resulting interaction strength $\Gamma(\omega)$ will have a narrow linewidth comb-like structure [39] instead in frequency space, compared to the continuum case of an open ended waveguide, with the peak intensity enhanced by a factor of $\frac{2\mathcal{F}}{\pi}$. The comb-like structure in the electron energy loss spectrum results from the spectral property of the resonator that is non-local with respect to the interaction region, and is only accessible since the interaction is analyzed in the electron energy basis, whose state is also non-local in nature. However, in order to access these comb like features in an EELS experiment, the electron-cavity characteristic interaction time (determined by the measured electron ZLP) has to be longer than the round trip time of the resonator, thus satisfying the energy-time uncertainty principle. Nonetheless, the comb-like structure can always be accessed from the optical side with a measurement time longer than the round trip time, as was shown in [39]. There is no difference in the total number of deposited quanta in a given mode family for the open waveguide case and the resonator case, as long as the the phase-matching bandwidth $\Delta\nu$ is much larger than $\Delta\nu_{\mathrm{FSR}}$. The total interaction strength $|g_m|^2$ of a mode family will be altered by the resonator structure when the phase-matching bandwidth $\Delta\nu$ is on the frequency scale of one FSR. The minimum number of modes inside the phase-matching bandwidth can be estimated with $N \sim \frac{1}{|n_g - n_{\mathrm{eff}}|}$ (for common dielectric materials $\sim 5 - 20$), so in order to access the regime where the phase matching bandwidth is smaller than the FSR, one requires $|n_g - n_{\mathrm{eff}}| > 1$, which is generally very difficult to achieve with structures using only dielectric materials. However, with common dielectric structures and careful mode dispersion engineering, the regime $N = \mathcal{O}(1)$ where resonance structure has an impact is accessible.

The motivation of using a resonator instead of an open waveguide is that the optical resonance frequencies are more passively stable, and the wavepackets generated from each resonator mode are generally much longer than the optical pulse length enforced by the phase-matching bandwidth from an open waveguide, and have energy density enhanced by the cavity finesse at resonant frequencies. Therefore, resonators have advantages in experiments such as photon interference which require good wavepacket overlap, and second order coherence measurements which require optical frequency filtering.

[1] H. J. Kimble, The quantum internet, Nature **453**, 1023 (2008).

[2] D. Awschalom, K. K. Berggren, H. Bernien, S. Bhave, L. D. Carr, P. Davids, S. E. Economou, D. Englund, A. Faraon, M. Fejer, S. Guha, M. V. Gustafsson, E. Hu, L. Jiang, J. Kim, B. Korzh, P. Kumar, P. G. Kwiat, M. Lončar, M. D. Lukin, D. A. Miller, C. Monroe, S. W. Nam, P. Narang, J. S. Orcutt, M. G. Raymer, A. H. Safavi-Naeini, M. Spiropulu, K. Srinivasan, S. Sun, J. Vučković, E. Waks, R. Walsworth, A. M. Weiner, and Z. Zhang, Development of quantum interconnects (quics) for next-generation information technologies, PRX Quantum **2**, 017002 (2021).

[3] M. Mirhosseini, A. Sipahigil, M. Kalaee, and O. Painter, Superconducting qubit to optical photon transduction, Nature **588**, 599 (2020).

[4] R. W. Andrews, R. W. Peterson, T. P. Purdy, K. Cicak, R. W. Simmonds, C. A. Regal, and K. W. Lehnert, Bidirectional and efficient conversion between microwave and optical light, Nature Physics **10**, 321 (2014).

[5] A. Sipahigil, R. E. Evans, D. D. Sukachev, M. J. Burek, J. Borregaard, M. K. Bhaskar, C. T. Nguyen, J. L. Pacheco, H. A. Atikian, C. Meuwly, R. M. Camacho, F. Jelezko, E. Bielejec, H. Park, M. Lončar, and M. D.

Lukin, An integrated diamond nanophotonics platform for quantum-optical networks, Science **354**, 847 (2016).
[6] N. H. Wan, T.-J. Lu, K. C. Chen, M. P. Walsh, M. E. Trusheim, L. De Santis, E. A. Bersin, I. B. Harris, S. L. Mouradian, I. R. Christen, E. S. Bielejec, and D. Englund, Large-scale integration of artificial atoms in hybrid photonic circuits, Nature **583**, 226 (2020).
[7] G. S. MacCabe, H. Ren, J. Luo, J. D. Cohen, H. Zhou, A. Sipahigil, M. Mirhosseini, and O. Painter, Nano-acoustic resonator with ultralong phonon lifetime, Science **370**, 840 (2020), https://www.science.org/doi/pdf/10.1126/science.abc7312.
[8] R. Riedinger, A. Wallucks, I. Marinković, C. Löschnauer, M. Aspelmeyer, S. Hong, and S. Gröblacher, Remote quantum entanglement between two micromechanical oscillators, Nature **556**, 473 (2018).
[9] C. Monroe, R. Raussendorf, A. Ruthven, K. R. Brown, P. Maunz, L.-M. Duan, and J. Kim, Large-scale modular quantum-computer architecture with atomic memory and photonic interconnects, Phys. Rev. A **89**, 022317 (2014).
[10] B. Brandstätter, A. McClung, K. Schüppert, B. Casabone, K. Friebe, A. Stute, P. O. Schmidt, C. Deutsch, J. Reichel, R. Blatt, and T. E. Northup, Integrated fiber-mirror ion trap for strong ion-cavity coupling, Review of Scientific Instruments **84**, 123104 (2013), https://doi.org/10.1063/1.4838696.
[11] I. Shomroni, S. Rosenblum, Y. Lovsky, O. Bechler, G. Guendelman, and B. Dayan, All-optical routing of single photons by a one-atom switch controlled by a single photon, Science **345**, 903 (2014), https://www.science.org/doi/pdf/10.1126/science.1254699.
[12] T. G. Tiecke, J. D. Thompson, N. P. de Leon, L. R. Liu, V. Vuletić, and M. D. Lukin, Nanophotonic quantum phase switch with a single atom, Nature **508**, 241 (2014).
[13] M. Brekenfeld, D. Niemietz, J. D. Christesen, and G. Rempe, A quantum network node with crossed optical fibre cavities, Nature Physics **16**, 647 (2020).
[14] B. Barwick, D. J. Flannigan, and A. H. Zewail, Photon-induced near-field electron microscopy, Nature **462**, 902 (2009).
[15] F. J. García de Abajo, Optical excitations in electron microscopy, Reviews of Modern Physics **82**, 209 (2010).
[16] A. Yurtsever, R. M. van der Veen, and A. H. Zewail, Subparticle Ultrafast Spectrum Imaging in 4D Electron Microscopy, Science **335**, 59 (2012).
[17] A. Feist, K. E. Echternkamp, J. Schauss, S. V. Yalunin, S. Schäfer, and C. Ropers, Quantum coherent optical phase modulation in an ultrafast transmission electron microscope, Nature **521**, 200 (2015).
[18] L. Piazza, T. Lummen, E. Quiñonez, Y. Murooka, B. Reed, B. Barwick, and F. Carbone, Simultaneous observation of the quantization and the interference pattern of a plasmonic near-field, Nature Communications **6**, 6407 (2015).
[19] K. Wang, R. Dahan, M. Shentcis, Y. Kauffmann, A. Ben Hayun, O. Reinhardt, S. Tsesses, and I. Kaminer, Coherent interaction between free electrons and a photonic cavity, Nature **582**, 50 (2020).
[20] Y. Kurman, R. Dahan, H. H. Sheinfux, K. Wang, M. Yannai, Y. Adiv, O. Reinhardt, L. H. G. Tizei, S. Y. Woo, J. Li, J. H. Edgar, M. Kociak, F. H. L. Koppens, and I. Kaminer, Spatiotemporal imaging of 2D polariton wave packet dynamics using free electrons, Science **372**, 1181 (2021).
[21] M. Liebtrau, M. Sivis, A. Feist, H. Lourenço-Martins, N. Pazos-Pérez, R. A. Alvarez-Puebla, F. J. G. de Abajo, A. Polman, and C. Ropers, Spontaneous and stimulated electron–photon interactions in nanoscale plasmonic near fields, Light: Science & Applications **10**, 82 (2021).
[22] M. Kociak and L. Zagonel, Cathodoluminescence in the scanning transmission electron microscope, Ultramicroscopy **176**, 112 (2017).
[23] A. Polman, M. Kociak, and F. J. García de Abajo, Electron-beam spectroscopy for nanophotonics, Nature Materials **18**, 1158 (2019).
[24] F. J. García de Abajo and V. Di Giulio, Optical Excitations with Electron Beams: Challenges and Opportunities, ACS Photonics , acsphotonics.0c01950 (2021), arXiv:2010.13510.
[25] O. Kfir, H. Lourenço-Martins, G. Storeck, M. Sivis, T. R. Harvey, T. J. Kippenberg, A. Feist, and C. Ropers, Controlling free electrons with optical whispering-gallery modes, Nature **582**, 46 (2020).
[26] N. Müller, V. Hock, H. Koch, N. Bach, C. Rathje, and S. Schäfer, Broadband Coupling of Fast Electrons to High-Q Whispering-Gallery Mode Resonators, ACS Photonics , acsphotonics.1c00456 (2021), arXiv:2103.13276.
[27] Y. Auad, C. Hamon, M. Tencé, H. Lourenço-Martins, V. Mkhitaryan, O. Stéphan, F. J. García de Abajo, L. H. G. Tizei, and M. Kociak, Unveiling the Coupling of Single Metallic Nanoparticles to Whispering-Gallery Microcavities, Nano Letters **22**, 319 (2022).
[28] E. Pomarico, I. Madan, G. Berruto, G. M. Vanacore, K. Wang, I. Kaminer, F. J. García de Abajo, and F. Carbone, meV Resolution in Laser-Assisted Energy-Filtered Transmission Electron Microscopy, ACS Photonics **5**, 759 (2018).
[29] J.-W. Henke, A. S. Raja, A. Feist, G. Huang, G. Arend, Y. Yang, F. J. Kappert, R. N. Wang, M. Möller, J. Pan, J. Liu, O. Kfir, C. Ropers, and T. J. Kippenberg, Integrated photonics enables continuous-beam electron phase modulation, Nature **600**, 653 (2021).
[30] K. E. Priebe, C. Rathje, S. V. Yalunin, T. Hohage, A. Feist, S. Schäfer, and C. Ropers, Attosecond electron pulse trains and quantum state reconstruction in ultrafast transmission electron microscopy, Nature Photonics **11**, 793 (2017), arXiv:1706.03680.
[31] O. Kfir, Entanglements of Electrons and Cavity Photons in the Strong-Coupling Regime, Physical Review Letters **123**, 103602 (2019).
[32] V. Di Giulio, M. Kociak, and F. J. G. de Abajo, Probing quantum optical excitations with fast electrons, Optica **6**, 1524 (2019), arXiv:1905.06887.
[33] A. Ben Hayun, O. Reinhardt, J. Nemirovsky, A. Karnieli, N. Rivera, and I. Kaminer, Shaping quantum photonic states using free electrons, Science Advances **7**, eabe4270 (2021).
[34] S. V. Yalunin, A. Feist, and C. Ropers, Tailored high-contrast attosecond electron pulses for coherent excitation and scattering, Physical Review Research **3**, L032036 (2021).
[35] M. Kozák, P. Beck, H. Deng, J. McNeur, N. Schönenberger, C. Gaida, F. Stutzki, M. Gebhardt, J. Limpert, A. Ruehl, I. Hartl, O. Solgaard, J. S. Harris, R. L. Byer, and P. Hommelhoff, Acceleration of sub-relativistic electrons with an evanescent optical wave at a planar interface, Optics Express **25**, 19195

(2017).
[36] R. Dahan, S. Nehemia, M. Shentcis, O. Reinhardt, Y. Adiv, X. Shi, O. Be'er, M. H. Lynch, Y. Kurman, K. Wang, and I. Kaminer, Resonant phase-matching between a light wave and a free-electron wavefunction, Nature Physics **16**, 1123 (2020), arXiv:1909.00757.
[37] D. K. Gramotnev and S. I. Bozhevolnyi, Plasmonics beyond the diffraction limit, Nature Photonics **4**, 83 (2010).
[38] F. J. García de Abajo and A. Howie, Relativistic electron energy loss and electron-induced photon emission in inhomogeneous dielectrics, Phys. Rev. Lett. **80**, 5180 (1998).
[39] A. Feist, G. Huang, G. Arend, Y. Yang, J. W. Henke, A. S. Raja, F. J. Kappert, R. N. Wang, H. Lourenço-Martins, Z. Qiu, J. Liu, O. Kfir, T. J. Kippenberg, and C. Ropers, Cavity-mediated electron-photon pairs (2022), arXiv:2202.12821 [quant-ph].
[40] M. H. P. Pfeiffer, C. Herkommer, J. Liu, H. Guo, M. Karpov, E. Lucas, M. Zervas, and T. J. Kippenberg, Octave-spanning dissipative kerr soliton frequency combs in si3n4 microresonators, Optica **4**, 684 (2017).
[41] J. Liu, G. Huang, R. N. Wang, J. He, A. S. Raja, T. Liu, N. J. Engelsen, and T. J. Kippenberg, High-yield, wafer-scale fabrication of ultralow-loss, dispersion-engineered silicon nitride photonic circuits, Nature Communications **12**, 2236 (2021).
[42] V. R. Almeida, R. R. Panepucci, and M. Lipson, Nanotaper for compact mode conversion, Opt. Lett. **28**, 1302 (2003).
[43] W. Bogaerts, D. Pérez, J. Capmany, D. A. B. Miller, J. Poon, D. Englund, F. Morichetti, and A. Melloni, Programmable photonic circuits, Nature **586**, 207 (2020).
[44] A. Politi, M. J. Cryan, J. G. Rarity, S. Yu, and J. L. O'Brien, Silica-on-silicon waveguide quantum circuits, Science **320**, 646 (2008), https://www.science.org/doi/pdf/10.1126/science.1155441.
[45] X. Bendaña, A. Polman, and F. J. García de Abajo, Single-Photon Generation by Electron Beams, Nano Letters **11**, 5099 (2011).
[46] H. T. Dung, L. Knöll, and D.-G. Welsch, Three-dimensional quantization of the electromagnetic field in dispersive and absorbing inhomogeneous dielectrics, Phys. Rev. A **57**, 3931 (1998).
[47] P. Milonni, *The Quantum Vacuum: An Introduction to Quantum Electrodynamics* (Elsevier Science, 1994).
[48] V. D. Giulio and F. J. G. de Abajo, Electron diffraction by vacuum fluctuations, New Journal of Physics **22**, 103057 (2020).
[49] O. Kfir, V. Di Giulio, F. J. G. de Abajo, and C. Ropers, Optical coherence transfer mediated by free electrons, Science Advances **7**, eabf6380 (2021).
[50] V. Di Giulio, O. Kfir, C. Ropers, and F. J. García de Abajo, Modulation of Cathodoluminescence Emission by Interference with External Light, ACS Nano , acsnano.1c00549 (2021), arXiv:2101.07748.
[51] T. Gruner and D.-G. Welsch, Green-function approach to the radiation-field quantization for homogeneous and inhomogeneous kramers-kronig dielectrics, Phys. Rev. A **53**, 1818 (1996).
[52] R. H. Ritchie and A. Howie, Inelastic scattering probabilities in scanning transmission electron microscopy, Philosophical Magazine A **58**, 753 (1988), https://doi.org/10.1080/01418618808209951.
[53] R. H. Ritchie, Plasma losses by fast electrons in thin films, Phys. Rev. **106**, 874 (1957).
[54] R. J. Glauber and M. Lewenstein, Quantum optics of dielectric media, Phys. Rev. A **43**, 467 (1991).
[55] K. J. Blow, R. Loudon, S. J. D. Phoenix, and T. J. Shepherd, Continuum fields in quantum optics, Phys. Rev. A **42**, 4102 (1990).
[56] B. Brecht, D. V. Reddy, C. Silberhorn, and M. G. Raymer, Photon temporal modes: A complete framework for quantum information science, Phys. Rev. X **5**, 041017 (2015).
[57] M. G. Raymer and I. A. Walmsley, Temporal modes in quantum optics: then and now, Physica Scripta **95**, 064002 (2020).
[58] C. W. Gardiner and M. J. Collett, Input and output in damped quantum systems: Quantum stochastic differential equations and the master equation, Phys. Rev. A **31**, 3761 (1985).